Remote Sensing of Cloud Properties Using MODIS Airborne Simulator Imagery During SUCCESS. II. Cloud Thermodynamic Phase

Bryan A. Baum[1]

Peter F. Soulen[2,4]

Kathleen I. Strabala[3]

Michael D. King[4]

Steven A. Ackerman[3]

W. Paul Menzel[5]

Ping Yang[6]

Submitted: May, 1999

Revised: September, 1999

For publication in the
Journal of Geophysical Research

[1] NASA Langley Research Center, Hampton, VA 23681-0001
[2] Joint Center for Earth Systems Technology, University of Maryland, Baltimore County
[3] Cooperative Institute for Meteorological Satellite Studies (CIMSS), Madison, WI, 53706
[4] NASA Goddard Space Flight Center, Greenbelt, MD 20771
[5] NOAA/NESDIS Advanced Satellite Product Team, Madison, WI 53706
[6] Science Systems and Applications, Inc., Lanham, MD 20706

Corresponding author: Dr. Bryan A. Baum, NASA/CIMSS, 1225 W. Dayton Street, Madison, WI 53706
Phone: (608) 263-3898, Fax: (608) 262-5974, Email: bryan.baum@ssec.wisc.edu

Abstract

Methods to infer cloud thermodynamic phase (ice or water) are investigated using multispectral imagery. An infrared (IR) trispectral algorithm using the 8.52, 11, and 12 μm channels [*Ackerman et al.* 1990; *Strabala et al.* 1994] forms the basis of this work and will be applied to data from the Earth Observing System (EOS) Moderate Resolution Imaging Spectroradiometer (MODIS) instrument. Since the algorithm uses IR channels, it can be applied to either daytime or nighttime data and is not sensitive to the presence of cloud shadows. A case study analysis is performed with a MODIS Airborne Simulator (MAS) scene collected during the Subsonic Aircraft: Contrail and Cloud Effects Special Study (SUCCESS) on April 21, 1996 at 2000 UTC. The scene under scrutiny is quite complex, containing low-level broken water clouds, cirrus cells, cloud shadows, subvisual cirrus, and contrails. The IR trispectral algorithm is found to be less accurate in (a) regions where more than one cloud phase type occurs, and (b) regions of thin cirrus overlying a lower-level cloud layer.

To improve the phase retrieval accuracy in these areas of difficulty, additional channels located at 0.65, 1.63, and 1.90 μm are incorporated. Radiative transfer (RT) calculations are performed to simulate the MAS channels using the cirrus and water cloud models detailed in *Baum et al.* [2000]. The RT calculations are performed for single-layer cirrus- and water-phase clouds as well as for the case of thin cirrus overlying a lower-level water droplet cloud. Both modeled results and application of the theory to a case study data suggest that the cloud thermodynamic phase retrieval accuracy can be improved by inclusion of the VIS/NIR channels.

1. Introduction

When the Moderate Resolution Imaging Spectroradiometer (MODIS) launches on the Earth Observing System (EOS) Terra platform (in late 1999), the data will be processed to derive a variety of products that include aerosol, cloud, and clear-sky properties [*King et al.*, 1992]. To derive cloud products, the data will be analyzed first to discriminate the clear from cloudy observations. Cloud top properties including height, temperature and emissivity will be calculated from cloudy radiance observations. Finally, cloud height retrievals and radiative transfer (RT) calculations will be used to infer cloud thermodynamic phase, cloud optical thickness (τ), and cloud particle size. The purpose of this work is to prepare algorithms that infer cloud thermodynamic phase using data collected from an aircraft radiometer called the MODIS Airborne Simulator (MAS) during the Subsonic Aircraft: Contrail and Cloud Effects Special Study (SUCCESS) [cf. Part I of this study].

The basis for our methodology is the trispectral infrared (IR) channel algorithm suggested by *Ackerman et al.* [1990], *Strabala et al.* [1994], and *Menzel and Strabala* [1997]. One strength of this method is that, as with any IR technique, it can be used for both daytime and nighttime retrievals. The daytime retrieval of cloud thermodynamic phase can be improved by incorporating the 0.65, 1.63, and 1.90-μm channels. The theoretical basis for these channel selections is provided in Section 2. Comparisons of RT calculations to MAS measurements [*King et al.* 1996] from the NASA ER-2 aircraft during SUCCESS are provided in Section 3. The behavior of the trispectral IR algorithm and the multispectral cloud thermodynamic phase results are investigated for the cases of low-level water droplet clouds, thin cirrus, and thin cirrus overlaying lower-level water droplet clouds. Section 4 presents the summary and conclusions of this study.

2. Physical Basis for Cloud Thermodynamic Phase Discrimination

2.1 The MAS trispectral infrared channels (8.52, 11, 12 μm)

The physical principles guiding the use of the 8.52, 11, and 12 μm channels for discriminating liquid water from ice clouds depend upon the bulk and single-scattering properties of water droplets and ice crystals. A brief examination of cloud particle absorption and scattering properties follows.

Radiative properties of clouds are determined by their geometric characteristics and their single-scattering properties. Single-scattering properties of cloud particles are defined by the complex index of refraction ($m = m_r - im_i$), the particle size distribution, and the particle shape distribution. The relationship between the particle single scattering properties and cloud absorption and emission can be described by the absorption coefficient κ which is a function of wavelength and m_i according to

$$\kappa = \frac{4\pi m_i}{\lambda}. \qquad (1)$$

Examination of m_i will provide a reasonable estimate of the magnitude of particle absorption.

The values of m_i for water and ice are shown in Fig. 1 for wavelengths between 8 and 13 μm. *Gosse et al*. [1995] provide the most recent measured data of the ice refractive index and are supplemented by the data published in *Warren* [1984]. The water refractive indices are from *Downing and Williams* [1975]. The magnitude of m_i for ice and water are nearly equal between 8.5 and 10 μm but diverge between 10 and 13 μm. If water and ice clouds were to have the same temperature (i.e., be at the same altitude), and have similar microphysical size and shape

distributions, the 8.52-μm cloud radiance would not depend greatly on thermodynamic phase. However, one would expect differences in the measured radiances between the ice and water cloud at 11 and 12 μm as ice has greater values of m_i than water.

The divergence in m_i at wavelengths greater than 9.5 μm forms the basis for the trispectral technique to infer particle thermodynamic phase; this was suggested by *Ackerman et al.* [1990], *Strabala et al.* [1994], and *Menzel and Strabala* [1997]. The absorption coefficient κ increases more between 8 and 11 μm than between 11 and 12 μm for ice, but the opposite is true for water. *Strabala et al.* [1994] demonstrated that radiances of ice clouds and water clouds tend to separate when brightness temperature differences (BTD) between 8.5 μm and 11 μm (BTD[8.5-11]) and 11 μm and 12 μm (BTD[11-12]) are compared. Ice clouds tend to have greater values of BTD[8.5-11] than BTD[11-12] whereas water clouds tend to have greater BTD[11-12] than BTD[8.5-11] values.

Cloud single scattering properties also depend on the assumed size distribution of the cloud particles. Tables 1 and 2 show the values of the single scattering albedo (ω_o) as a function of particle size for water and ice clouds, respectively. Examination of the last three columns of Table 1 shows that ω_o is much larger at 8.52 μm than at 11 or 12 μm until values of r_{eff} become large.

RT calculations of BTDs for liquid water and ice clouds are shown in Figure 2. The RT calculations are based on a temperature and humidity rawinsonde profile recorded on April 21, 1996 during SUCCESS [*Baum et al.*, 2000]. The low-level water phase cloud has a cloud-top temperature of 284 K while the cirrus cloud has a temperature of 235 K. Results are presented in the form of BTD[8.52-11] and BTD[11-12] as a function of the 11-μm brightness temperature. Visible (0.65 μm) optical thicknesses are superimposed in the figure as a reference. There are

several points to emphasize. First, the BTD[8.52-11] values for the five water droplet cloud models are less than zero (Fig. 2a). However, the BTD[8.52-11] values for cirrus are primarily greater than zero for optical thicknesses (τ) between 0.5 and 10 (Fig. 2c). Second, the BTD[11-12] values for water (Fig. 2b) and ice (Fig. 2d) clouds are very similar. Third, one may note that the BTD[8.52-11] curves for the various r_{eff} are not monotonically increasing as a function of size (Fig. 2a) as are the BTD[11-12] results (Fig. 2b). In fact, there seem to be multiple particle size solutions for BTD[8.52-11] values when $\tau > 1$ and $\tau < 10$. Fourth, for water clouds, the range of BTD[11-12] values is larger than BTD[8.52-11] for all but the largest r_{eff}. Conversely, for ice clouds, the range of BTD[8.52-11] values is larger than BTD[11-12]. This suggests the possibility of using these cloud signals to determine cloud phase for all but the largest of cloud ice and water particles.

2.2 The MAS Solar and Near-Infrared channels (0.65, 1.63, 2.15 μm)

Fig. 3 shows that liquid water and ice have very small values of m_i for wavelengths less than about 0.7 μm, so clouds composed of either liquid or ice absorb very little solar radiation at visible wavelengths. At 1.63 μm, the m_i values for water and ice increase over those at 0.65 μm and diverge, with m_i for ice being greater than m_i for water. Therefore, one could infer that if particles in water and ice clouds had similar size and shape distributions, the 0.65-μm cloud reflectance would not depend greatly upon thermodynamic phase, while one would expect the 1.63-μm cloud radiances for ice clouds to be less than those for similar liquid water clouds. However, because the values of m_i for ice and liquid water are almost equal at 2.15 μm, the 2.15-μm radiances would offer less contrast between ice and water than those for the 1.63 μm channel.

For an infinitely deep cloud layer composed of 5-μm spheres, absorption by an ice cloud at 1.6 microns would be about twice the absorption by a water cloud [*Pilewskie and Twomey* 1987a, 1987b].

The size distribution also affects the single scattering properties and hence the cloud reflectance. Results for a modified gamma distribution of spherical water droplets are presented in the first two columns of Table 1. As the effective radius of the size distribution increases, the values for single-scattering albedo ω_o decrease. Further, the values of ω_o are lower at 2.15 μm than at 1.63 μm for the same size distribution since there is more absorption at the longer wavelength. *Hansen and Pollack* [1970] and *Curran and Wu* [1982] have performed similar calculations for clouds composed of spheres of liquid water and ice.

Single-scattering albedos at 1.63 and 2.15 μm as a function of cirrus model effective size are presented in Table 2 for nonspherical ice crystals. As explained in Part I, the cirrus effective size is based on the ratio of total volume to total projected area of the irregularly shaped crystals. The values of ω_o decrease monotonically with increasing effective size over this cloud particle size range, suggesting that the cloud reflectance should decrease with increasing particle size. The values of ω_o are typically higher for the clouds composed of water droplets (Table 1) than for clouds composed of ice crystals at similar sizes (Table 2), suggesting that water droplet clouds can be expected to exhibit higher reflectances at 1.63 and 2.15 μm than ice clouds having the same optical thickness.

Little is known about how the particle shape distribution affects the scattering properties, especially for cirrus clouds that may be composed of very irregular shapes. Calculations by *Liou* [1974] and *Stephens* [1980a, 1980b] suggest that nonspherical shapes make only a slight modification to ω_o of equivalent-volume spheres, but that the magnitude of g is depressed.

Sensitivity studies are planned to further assess how a cloud particle shape distribution affects cloud reflectance.

RT calculations at 1.63 and 2.15 μm for water and ice clouds are presented as a function of the 0.65-μm reflectance (Figure 4) and 11-μm brightness temperature (Figure 5), using the methodology in Part I [*Baum et al.*, 2000]. The April 21, 1996 rawinsonde profile (see Part I) was used in the calculations. The water cloud has a cloud-top temperature of 284 K while the cirrus cloud has a temperature of 235 K. Visible (0.65 μm) optical thicknesses are provided in the figure as a reference. Reflectances of clouds composed of water droplets are presented in Fig. 4(a,b) and Fig. 5(a,b), while reflectances of cirrus clouds are presented in Fig. 4(c,d) and Fig. 5(c,d).

The 1.63 and 2.15 μm reflectances (Figs. 4a and 4b) increase monotonically as a function of optical thickness from the clear-sky value for $r_{eff} < 8$ μm. As r_{eff} increases from 8 μm, the 1.63 and 2.15 μm reflectances change little with increasing optical thickness. A comparison with the reflectances for ice clouds (Figs. 4c and 4d) indicates that both 1.63 and 2.15-μm reflectances tend to be lower for ice clouds than for water clouds. We note that for clouds of low optical thickness, there is little to distinguish between the various water or ice models.

For a water phase cloud with $r_{eff} > 8$ μm, the results in Fig. 5a indicate that the 1.63 μm reflectances are relatively insensitive to optical thickness for $\tau < 5$. For $\tau \sim 5$, the 11-μm brightness temperature has nearly reached the actual temperature of the cloud (284 K) and the reflectance tends to increase with increasing τ for all effective radii except $r_{eff} > 32$ μm. Fig. 5b indicates that water cloud reflectance at 2.15 μm depends more on r_{eff}. For $r_{eff} = 32$ μm, the 2.15-μm water cloud reflectances decrease with increasing τ.

For all the cirrus models, RT calculations (Figs. 5c and 5d) for $\tau < 5$ indicate an almost

linear relationship between 1.63 or 2.15 μm reflectance and 11-μm brightness temperature (BT). For a given τ, the reflectances decrease monotonically with increasing cloud particle effective size. For this set of cirrus models, the reflectances do not tend to increase at higher optical thickness ($\tau > 5$) as much as those for some of the water cloud models.

A comparison of the water cloud 1.63 or 2.15 μm reflectances with their respective cirrus counterparts shows that there are cases where one could expect an unambiguous distinction between water and ice phase clouds. For example, the reflectances calculated from the Ci Uncinus model at high optical thicknesses are much less than the water cloud reflectances from any of the models presented here.

2.3 *Use of the strongly absorbing water vapor channel (1.90 μm)*

The potential for improving cirrus detection by using a channel near a band of strong water vapor absorption, such as at 1.38 μm, has been demonstrated by *Gao et al.* [1993]. The presence of water vapor attenuates the incoming solar radiation to such a degree that aircraft or satellite instrument measurements at 1.38 μm will receive little scattered solar radiance from the earth's surface or low clouds. Cirrus clouds are located generally at altitudes above 7 km in midlatitude and 9 km in tropical regions [*Liou*, 1986]. Because of their high altitude, cirrus lie above more than 90% of the atmospheric water vapor, allowing the 1.38 μm water vapor channel to receive an increased amount of scattered solar energy.

In addition to the 1.38 μm band, other bands of strong water vapor absorption include 0.72, 0.81, 0.94, 1.14, 1.87, 2.7, 3.4, and 6.3 μm [*Kratz and Cess*, 1985]. The MAS 1.90-μm channel is ideally suited as a high-level cloud detection channel and can aid daytime phase discrimination. RT calculations for ice- and water-phase clouds of reflectances at 1.90 μm as a function of cloud height are shown in Figs. 6a and 6b, respectively. A cold cirrus model is employed for the ice

cloud calculations, while a water cloud is modeled as a modified gamma distribution having an r_{eff} = 4 μm [*Baum et al.*, 2000]. Visible (0.65 μm) optical thicknesses range from 0 to 20 for the cirrus calculations and from 0 to 50 for the water cloud calculations.

The results in Fig. 6 indicate that cloud reflectance at 1.90-μm is indeed a strong function of cloud height; the reflectances increase with cloud optical thickness and cloud altitude (decreasing cloud-top temperature). As the cloud altitude decreases, increasing water vapor absorption causes a decrease in 1.90-μm reflectance. For a midlatitude summer time atmospheric profile typical of the SUCCESS time period, the 1.90-μm channel will not be sensitive to clouds below 3 km (cloud-top temperatures within 18 K of the surface temperature). The RT calculations indicate that 1.90-μm channel cloud reflectances can become significantly higher than clear-sky reflectances (near 300 K in Figs 6a and 6b) for supercooled water-phase clouds when the cloud temperature decreases below 260 K. This being the case, the 1.90-μm channel should be useful for the detection of both supercooled water phase clouds and ice-phase clouds. Based on these results, it would be inaccurate to assume that a 1.90-μm reflectance much greater than that for clear-sky conditions is caused solely by ice phase clouds.

2.4 *Effect of Thin Cirrus Overlying Low-Level Clouds*

Previous methods to infer the cloud thermodynamic phase assume *a priori* that there is only a single, well-defined cloud layer in the atmospheric column. However, multilayered clouds have been found to occur in about half of all ground-based cloud observations [*Hahn et al.* 1982, 1984; *Warren et al.* 1985]. These cloud overlap conditions can confuse phase identifications. One example of this is when thin cirrus overlies a lower level water cloud.

To illustrate this, we investigate the remote sensing problem of cirrus [T = 234 K] overlying a water phase cloud with fixed properties: T = 284 K, r_{eff} = 4 μm, and τ = 5. Calculations are

presented in Figure 7 for reflectances at 1.63 and 2.15 μm as well as for BTD[8.52-11] and BTD[11-12]. One curve in each of the frames represents RT calculations performed for the single layered water cloud (WC); the remaining curves are results for cirrus overlying the WC layer. Visible (0.65-μm) optical thicknesses (τ) are provided for reference along the WC and cirrus over WC curves; the τ values for overlapped cloud curves are for the cirrus cloud layer alone and do not represent the total column τ.

Several observations can be made from comparison of Fig. 7 (cirrus above water cloud) with Fig. 2 and Fig. 5 (single-layered water or ice cloud, respectively). First, for cirrus $\tau < 10$, the presence of the lower cloud tends to increase both the 1.63 and 2.15 μm reflectances over those for cirrus alone. Second, the presence of the lower cloud acts to lower both the BTD[8.52-11] and BTD[11-12] values over those for cirrus alone. For example, the BTD[8.52-11] for the single-level Ci (cold) model with $\tau_{ci} = 3$ is 4 K (Fig. 2c), but 3 K for Ci (cold) over a lower water cloud (Fig. 7c). However, the range of BTD[8.52-11] values is still greater than the range of BTD[11-12] values, suggesting that the cirrus cloud is contributing more to the radiance observed than the water cloud. For $\tau > 5$, the presence of the lower water cloud has minimal effect.

For very thin cirrus ($\tau < 0.5$) overlying a lower water cloud, one may note that (a) the calculated reflectance or BTD values for each of the cirrus models show little dependence on effective particle size, and (b) the calculated 11-μm BT is still above 273 K. While the 1.63 or 2.15 μm reflectances for the case of very thin cirrus overlap do not differ significantly from that of the water cloud alone, the 11-μm BT is lower. Since the BTD values decrease when a lower cloud layer is present under the cirrus from those calculated for cirrus alone, the interpretation of the measurements becomes problematic. For example, the reflectance measurements could be misinterpreted to conclude that only a thicker ice cloud layer were present, rather than a

multilayer cloud system where a thin cirrus cloud hovers above a thick water cloud. We present a straightforward method to infer when thin cirrus might be overlying a lower-level cloud in *Baum and Spinhirne* [2000].

3. Methodology for Retrieval of Cloud Thermodynamic Phase

a. The MAS IR trispectral method

As described in *Strabala et al.* [1994], the essence of the trispectral technique to determine cloud thermodynamic phase consists of interpreting a scatter diagram of BTD[8.52-11] versus BTD[11-12]. Water and ice cloud tend to separate in distinct clusters with ice clouds tending to group in line with a slope greater than one, and water cloud in a group with a slope less than one, with mixed phase clouds filling in between. This is due primarily to the effects of the indices of refraction of ice and water across this spectral region as discussed in Section 2.1. Ice and water cloud with visible optical thicknesses between 1 and 5 (Fig. 2) are discerned by large positive values of BTD[8.52-11] and BTD[11-12].

The trispectral technique is described in detail in the MODIS Algorithm Theoretical Basis Document (ATBD) [*Menzel and Strabala*, 1997]. It first attempts to identify single phase cloud scenes by a characteristic pattern in the BTD scatter diagram. If this is not possible, it attempts to identify cloud phase by the pixel locations in reference to the unity slope in the brightness temperature difference scatter diagram (i.e., where BTD[8.52-11] equals BTD[11-12]).

The MAS trispectral technique is implemented in the following manner. In the preprocessing stage, the MAS cloud masking algorithm is applied to the scene and each pixel is classified as being in one of four categories: confident clear, probably clear, undecided, and cloudy [*Ackerman et al.* 1998]. After identifying the clear-sky data in the scene, the MAS data are averaged over *10 x 10* pixel arrays, or boxes. The mean and standard deviation is determined separately for the clear

and cloudy pixels within each box. Finally, the BTD[8.52-11] and BTD[11-12] are calculated using the average clear/cloud values for the box.

A cluster analysis is performed to identify boxes containing opaque clouds using the 11-μm data. This analysis is similar in concept to the spatial coherence method [*Coakley*, 1983]. The thermodynamic phase of the boxes within each cluster is determined by checking the proximity of the cluster center to the unity slope in the BTD scatter diagram (i.e., the scatterplot of BTD[8.52-11] vs. BTD[11-12]). If the center lies above the unity slope, every box within the cluster is labeled as an opaque ice cloud; if below the center, every box is labeled as an opaque water cloud. If the cluster center has an 11-μm BT less than 230 K, the boxes within the cluster are immediately classified as containing ice.

At this point, most boxes are classified as of type clear sky, opaque ice cloud, or opaque water cloud. The next step is to identify a single phase single-layered cloud scene based upon the range of BTDs in the scene. A maximum likelihood estimator (MLE) is performed on all unclassified boxes that have an 11-μm BT greater than 255 K. Figs. 2c and 2d illustrate how the values of BTD[8.52-11] and BTD[11-12] of the cirrus clouds rise in a fairly uniform manner as τ increases until reaching a peak at around 3, corresponding to an 11-μm BT ~ 260K. It is this slope of BTDs going from low τ to a cutoff optical thickness that the MLE uses to identify a single phase cloud for the entire scene. If the sensitivity of the MLE is set correctly, an accurate line fit can be made to a water cloud scene of varying optical depths (Fig. 2a and 2b) without a cutoff, because the range of values are smaller than those observed for ice cloud. If an acceptable linear fit is found to the data in the scatter diagram of BTD[8.52-11] versus BTD[11-12] using 11-μm BTs > 255 K, then the entire scene is classified as ice if the slope of the fitted line is greater than 1 and no opaque water cloud was found previously, or it is classified as water cloud if the slope is less than

1 and no opaque ice cloud was found previously.

The maximum likelihood estimator used is

$$\chi^2 = \left(\frac{1}{\sigma_x^2 + \sigma_y^2}\right)\sum_{i=1}^{N}\frac{(y_i - mx_i - b)^2}{(1 - m^2)}, \tag{2}$$

where σ_x^2 and σ_y^2 are the errors in both the *x* (BTD[11-12]) and *y* (BTD[8.5-11]) directions. The values of σ_x^2 and σ_y^2 used are 0.35K and 0.30 K, respectively as determined for the MAS during the TOGA/COARE experiment. *N* is the number of boxes used in the analysis, *b* is the intercept, and *m* is the slope. To determine the χ^2, one sums the squared distances from each measured point to the point of the line from which it is most likely to have been produced (perpendicular point). If χ^2 is small (dependent upon the number of boxes used in the MLE), and the goodness of fit satisfies a gamma distribution, then the slope is tested for clouds composed of a single phase. If $m > 1$, the clouds are labeled as having an ice thermodynamic phase. If $m < 1$, the clouds are labeled as water phase as previously described.

If there are cloud-filled boxes as yet unclassified after application of the previous analysis, a multiphase cloud region is assumed. This could occur for a single cloud layer containing both ice and water, a processing region that contains non-overlapped ice and water phase clouds, or a region that contains thin cirrus overlying a lower level cloud. Each *10 x 10* pixel box is tested for its proximity to the unity slope. If the box lies within 0.3 K of the unity slope, it is flagged as cloud of uncertain thermodynamic phase.

Fig. 8 shows the results of applying this method to a MAS scene, specifically flight track 11 collected on April 21, 1996 during the SUCCESS field experiment. The portion of the flight track shown in Figs. 8a and 8b at 0.65 and 1.9 μm, respectively, shows a very complex cloud scene that

contains cumulus, cirrus, contrails, and overlapping clouds. The scale of the image is 37.5 km cross track by 50 km along track. At 0.65 μm, low-level water phase clouds appear bright and have smaller shadows than the cirrus, which have less distinct boundaries. The cirrus have a wispy appearance. At 1.9 μm, the source of the upwelling radiance is primarily from the upper troposphere. The 1.9-μm image clearly shows the presence of two contrails and the presence of cirrus more clearly than the 0.65-μm image. The associated MAS cloud mask [*Ackerman et al.*, 1998] is provided in Fig. 8c for a portion of the scene. Specifically, the areas outlined as being cloudy are called either "cloudy" or "uncertain" by the MAS cloud mask. Most of the scene is covered in cloud. One may note that cloud shadows are present in the clear-sky areas.

Thermodynamic cloud phase retrievals for this scene are presented in Figure 9 for imager data within a viewing angle of 30° of nadir. The viewing angle is limited because we have not yet included additional logic in the algorithm to accomodate the increase in water vapor absorption for each channel. Fig. 9a shows the results of application of the IR trispectral method. Boxes (i.e., *10x10* pixel arrays) are painted blue for water phase clouds, magenta for ice phase cloud, and green for uncertain. The performance of the trispectral method is most accurate for single-layered clouds. The results of the algorithm are less accurate in areas containing (a) clouds of low optical thickness, such as the areas along the edges of the cirrus cells and the areas between the cirrus cells, and (b) thin cirrus overlying a lower level cloud. Because this scene contains more than one type of cloud, an acceptable linear fit to the data could not be made. Therefore, each box was assigned a cloud phase based upon its location with respect to the unity slope in the scatter diagram. From the modeled data of Figure 2c and 2d, we can see that thin ice cloud ($\tau < 0.5$) may be misidentified because the values of BTD[11-12] may be much greater than BTD[8.5-11].

b. Augmentation of the MAS IR trispectral method with the VIS/NIR channels

Based on the RT calculations presented earlier in Section 2, the trispectral algorithm may be augmented with additional tests using the VIS and NIR channel reflectances. Our intent is to improve the phase discrimination where multiphase, multilayer cloud scenes cause uncertain results, such as around the edges of cirrus cells.The first set of tests (Eqs. 3-6), to be applied to each pixel concurrently, is to determine low-level clouds composed of water droplets:

$$[\overline{BT_{cs}^{11}} - BT^{11}(measured)] > 18K \tag{3}$$

$$[\rho^{1.90}(measured) - \overline{\rho_{cs}^{1.90}}] < \sigma_{cs}^{1.90} \tag{4}$$

$$[\rho^{0.65}(measured) - \overline{\rho_{cs}^{0.65}}] > \sigma_{cs}^{0.65} \tag{5}$$

$$[\rho^{1.63}(measured) - \overline{\rho_{cs}^{1.63}}] > \sigma_{cs}^{1.63} \tag{6}$$

where BT^{11} is the brightness temperature at 11 μm, ρ^{λ} are measured reflectances from the imagery at wavelength λ, quantities with overbars are arithmetic means, and σ^{λ} are standard deviations of brightness temperatures or reflectances at wavelength λ of pixels from the imagery identified as clear-sky (subscript "cs") by the cloud-clearing algorithm. Eq. (3) states that any pixel identified as cloudy with an 11-μm BT within 18K (3 km of the surface assuming a lapse rate of 6 K/km) of the average 11-μm BT for clear-sky pixels is likely from a low-level cloud in the atmosphere, and therefore possibly a water cloud. Eq. (4) states that further confirmation of a low-level cloud occurs if the 1.90-μm reflectance is also very low in accordance with the analyses performed in Section 2.3. There, it was shown that water cloud reflectance at 0.65 and 1.63-μm increased with optical thickness. Additionally, if the differences between the 0.65 and 1.63-μm reflectances and their average clear sky reflectances are greater than one standard deviation of the average clear-sky reflectances (Eqs. 5 and 6), the pixel is classified as a water cloud.

A different set of tests (Eqs. 7-9) are employed for determination of ice-phase clouds. As indicated by the RT calculations, both the 11-μm brightness temperature and the 1.90-μm reflectance will increase above the background if there is a cloud well above the surface (differences between the brightness temperatures and the reflectances will be greater than one standard deviation of the average clear-sky values), but the 1.63-μm reflectance tends to decrease if ice-phase clouds are present because ice absorbs more than liquid water at that wavelength. All pixels that pass Eqs. 7-9 are classified as ice clouds:

$$[\overline{BT_{cs}^{11}} - BT^{11}(measured)] = \sigma_{cs}^{11} \tag{7}$$

$$[\rho^{1.90}(measured) - \rho_{cs}^{1.90}] > \sigma_{cs}^{1.90} \tag{8}$$

$$[\rho^{1.63}(measured) - \overline{\rho_{cs}^{1.63}}] < \sigma_{cs}^{1.63} \tag{9}$$

Phase discrimination for midlevel clouds (altostratus or altocumulus) involve a final set of tests. Such clouds may be composed of supercooled water droplets and often have 11-μm BT values as low as 233 K. Data that have not been classified as water or ice by the first two sets of tests are processed by Eqs. 10-12:

$$233K < BT^{11}(measured) < (\overline{BT_{cs}^{11}} - 18K) \tag{10}$$

$$[\rho^{1.90}(measured) - \overline{\rho_{cs}^{1.90}}] > \sigma_{cs}^{1.90} \tag{11}$$

$$[\rho^{1.63}(measured) - \overline{\rho_{cs}^{1.63}}] > \sigma_{cs}^{1.63} \tag{12}$$

If the result of application of Eqs. 10 and 11 is positive, the cloud lies above enough of the column water vapor so that scattering overcomes water vapor absorption. These two tests alone are not enough to discriminate cloud thermodynamic phase. Water clouds tend to display higher NIR

(1.63 μm) reflectances than ice clouds. If all three tests (Eqs. 10-12) are positive, the cloud is probably in the middle troposphere and composed of water droplets.

The results from application of both the trispectral IR method and the supplemental tests on the MAS scene of April 21 are displayed in Fig. 9b. More of the scene is now identified as ice clouds than in Fig. 9a. One complication in the analysis is that the NIR channels are very sensitive to the presence of cloud shadows, especially over land. Vegetated surfaces tend to be brighter in the NIR than in the visible wavelengths because of chlorophyll absorption at wavelengths below about 0.7 μm. Since the surface is brighter in the NIR, cloud shadows tend to increase the contrast between the surface and the cloud. If shadows are present, the NIR surface reflectance can decrease to half of the non-shadowed clear-sky reflectance. Thus, sensitivity to cloud shadows affects the average and standard deviation values of the clear-pixel reflectances. The average clear-sky reflectances decrease while the variance increases when shadows are present, making an accurate thermodynamic phase determination problematic for clouds with small optical thickness. Another problematic area occurs in regions where thin cirrus overlies a lower cloud layer. Some of the boxes now labeled as “ice” may also have low cloud present, i.e., overlapping cloud layers are present.

4. Summary and Conclusions

In this study we summarize a methodology for the inference of cloud thermodynamic phase. Radiative transfer calculations are performed to simulate the MAS 0.65, 1.63, 1.90, 2.15, 8.52, 11, and 12 μm channels using the cirrus/water cloud models detailed in *Baum et al*. [2000]. The RT

calculations are performed for single-layer cirrus- and water-phase clouds as well as for thin cirrus overlying lower-level water droplet cloud.

A case study analysis is performed with MAS data collected during SUCCESS on April 21, 1996 at 20:00 UTC. The scene under scrutiny is quite complex, containing low-level broken water clouds, cirrus cells, cloud shadows, subvisual cirrus, and contrails. We find that the IR trispectral algorithm [*Ackerman et al.* 1990; *Strabala et al.* 1994; *Menzel and Strabala* 1997] performs well for both water and ice clouds having a relatively high optical thickness ($\tau > 2$). The algorithm is less accurate for thin cirrus in scenes where more than one type of cloud are present, sometimes misclassifying thin cirrus as water-phase clouds. The advantages of the IR trispectral technique are that it can be applied to both daytime and nighttime data and is not sensitive to the presence of cloud shadows.

The IR trispectral method was augmented by adding tests using the 0.65, 1.63, and 1.90 μm channels, enhancing the ability to discriminate cloud thermodynamic phase and to identify thin cirrus clouds. Uncertainties are noted for regions containing cloud shadows, making the inference of phase problematic for regions containing clouds of low optical thickness. Another area of uncertainty is in regions containing thin cirrus overlying a lower layer cloud.

The following paper [*Baum and Spinhirne* 2000] suggests methodology for discerning thin cirrus overlying a lower-level cloud.

Acknowledgments

The authors would like to acknowledge the contributions of Chris Moeller and Liam Gumley at SSEC/CIMSS and the ER-2 and MODIS Airborne Simulator field teams. We appreciate the helpful suggestions from the two anonymous reviewers. This work was supported by a grant from the MODIS Science Team.

References

Ackerman, S. A., W. L. Smith, J. D. Spinhirne and H. E. Revercomb, The 27-28 October 1986 FIRE IFO cirrus case study: Spectral properties of cirrus clouds in the 8-12 μm window, *Mon. Wea. Rev.*, *118*, 2377-2388, 1990.

Ackerman, S. A., K. I. Strabala, W. P. Menzel, R. A. Frey, C. C. Moeller, and L. E. Gumley, Discriminating clear sky from clouds with MODIS, *J. Geophys. Res.*, *103*, 32141-32157, 1998.

Baum, B. A., D. P. Kratz, P. Yang, S. Ou, Y. Hu, P. F. Soulen, and S-C. Tsay, Remote sensing of cloud properties using MODIS Airborne Simulator imagery during SUCCESS. I. Data and models, *J. Geophys. Res.*, 2000, In press.

Baum, B. A. and J. D. Spinhirne, Remote sensing of cloud properties using MODIS Airborne Simulator imagery during SUCCESS. III. Cloud overlap, *J. Geophys. Res.*, 2000, *In press.*

Coakley, J. A., Jr., Properties of multilayered cloud systems from satellite imagery, *J. Geophys. Res.*, *88*, 10,818-10,828, 1983.

Curran, R. J., and M. L. C. Wu, Skylab near-infrared observations of clouds indicating supercooled liquid water droplets, *J. Atmos. Sci*., *39*, 635-647, 1982.

Downing, H. D., and D. Williams, Optical constants of water in the infrared, *J. Geophys. Res*., *80*, 1656-1661, 1975.

Gao, B-C., A. F. H. Goetz, and W. J. Wiscombe, Cirrus cloud detection from airborne imaging spectrometer data using the 1.38-μm water vapor band, *Geophys. Res. Letters*, *20*, 301-304, 1993.

Gosse, S., D. Labrie, and P. Chylek, Refractive index of ice in the 1.4-7.8 μm spectral range, *Appl. Opt*., *34*, 6582-6586, 1995.

Hahn, C. J., S. G. Warren, J. London, R. M. Chervin, and R. Jenne, Atlas of simultaneous occurrence of different cloud types over the ocean, *NCAR Technical Note, TN-201+STR*, 211 pp., National Center for Atmospheric Research, Boulder, Colorado, 1982.

Hahn, C. J., S. G. Warren, J. London, R. M. Chervin, and R. Jenne, Atlas of simultaneous occurrence of different cloud types over land, *NCAR Technical Note, TN-241+STR*, 209 pp., National Center for Atmospheric Research, Boulder, Colorado, 1984.

Hansen, J. E., and J. B. Pollack, Near-infrared light scattering by terrestrial clouds, *J. Atmos. Sci*, *27*, 265-281, 1970.

King, M. D., Y. J. Kaufman, W. P. Menzel, D. Tanre, Remote sensing of cloud, aerosol, and water vapor properties from the Moderate Resolution Imaging Spectrometer (MODIS), *IEEE Trans. on Geosci. Remote Sens*., *30*, 1-27, 1992.

King, M. D., W. P. Menzel, P. S. Grant, J. S. Myers, G. T. Arnold, S. E. Platnick, L. E. Gumley, S-C. Tsay, C. C. Moeller, M. Fitzgerald, K. S. Brown, and F. G. Osterwisch, Airborne scanning spectrometer for remote sensing of cloud, aerosol, water vapor, and surface properties, *J. Atmos. Oceanic Technol*., *13*, 777-794, 1996.

Kratz, D. P., and R. D. Cess, Solar absorption by atmospheric water vapor: a comparison of radiation models, *Tellus*, *37B*, 53-63, 1985.

Liou, K. N., On the radiative properties of cirrus in the window region and their influence on remote sensing of the atmosphere, *J. Atmos. Sci*., *31*, 522-532, 1974.

Liou, K. N., Influence of cirrus clouds on weather and climate processes: A global perspective, *Mon. Wea. Rev*., *114*, 1167-1199, 1986.

Menzel, W. P., and K. I Strabala, Cloud top properties and cloud phase algorithm theoretical basis document, MODIS Algorithm Theoretical Basis Document, 55 pp., 1997. [Available at http://eospso.gsfc.nasa.gov/atbd/modistables.html.]

Pilewskie, P., and S. Twomey, Discrimination of ice from water in clouds by optical remote sensing, *Atmos. Res*., *21*, 113-122, 1987a.

Pilewskie, P., and S. Twomey, Cloud phase discrimination by reflectance measurements near 1.6 and 2.2 μm, *J. Atmos. Sci*., *44*, 3419-3420, 1987b.

Stephens, G. L., Radiative properties of cirrus clouds in the infrared region, *J. Atmos. Sci*., *37*, 435-446, 1980a.

Stephens, G. L., Radiative transfer on a linear lattice, Application to anisotropic ice crystal clouds, *J. Atmos. Sci*., *37*, 2095-2104, 1980b.

Strabala, K. I., S. A. Ackerman and W. P. Menzel, Cloud properties inferred from 8-12 μm data, *J. Appl. Meteor*., *2*, 212-229, 1994.

Warren, S. G., Optical constants of ice from the ultraviolet to the microwave, *Appl. Opt*., *23*, 1206-1224, 1984.

Warren, S. G., C. J. Hahn, and J. London, Simultaneous occurrence of different cloud types, *J. Climate Appl. Meteor*., *24*, 658-667, 1985.

List of Tables

1. Single scattering albedo ω_o for water droplet clouds as a function of effective size and wavelength.

2. Single scattering albedo ω_o as a function of cirrus model effective size (μm) and wavelength.

Table 1: Single scattering albedo ω_o for water droplet clouds as a function of effective size and wavelength.

r_{eff}	ω_o (1.63 μm)	ω_o (2.15 μm)	ω_o (8.52 μm)	ω_o (11 μm)	ω_o (12 μm)
4	0.9976	0.9912	0.7459	0.2914	0.2218
8	0.9950	0.9806	0.7768	0.4400	0.3524
10	0.9939	0.9760	0.7550	0.4747	0.3871
16	0.9906	0.9635	0.6501	0.5151	0.4410
32	0.9824	0.9330	0.5348	0.5051	0.4815

Table 2: Single scattering albedo ω_o as a function of cirrus model effective size (μm) and wavelength

λ (μm)	m_r	m_i		Cs	Ci Uncinus	Ci (Cold)	Ci (Warm)	Ci (T=-20°C)	Ci (T=-40°C)	Ci (T=-60°C)
0.65	1.308	0.1365E-07	ω_o	0.999995	0.9999	0.999997	0.999994	0.999993	0.999992	0.999997
1.63	1.288	0.2529E-03	ω_o	0.9720	0.9055	0.9508	0.9643	0.9561	0.9508	0.9811
1.90	1.278	0.4108E-03	ω_o	0.9592	0.8713	0.9800	0.9497	0.9385	0.9310	0.9724
2.15	1.268	0.6858E-03	ω_o	0.9491	0.8443	0.9749	0.9382	0.9246	0.9154	0.9656
8.52	1.291	0.03909	ω_o	0.6966	0.5737	0.7574	0.6867	0.6659	0.6473	0.7344
11.01	1.103	0.2493	ω_o	0.4822	0.5373	0.4124	0.4761	0.4934	0.5044	0.4409
12.01	1.285	0.414	ω_o	0.5412	0.5678	0.5021	0.5339	0.5440	0.5501	0.5170

List of Figures

1. Imaginary indices of refraction for water (solid line) and ice (dotted line) over wavelengths ranging from 8 to 12 μm.

2. Radiative transfer model results for (a) the BTD[8.5-11 μm] versus the 11-μm brightness temperature for clouds composed of water droplets; (b) the BTD[11-12 μm] versus the 11-μm brightness temperature for clouds composed of water droplets; (c) the BTD[8.5-11 μm] versus the 11-μm brightness temperature for cirrus (ice) clouds; and (d) the BTD[11-12 μm] versus the 11-μm brightness temperature for cirrus (ice) clouds.

3. Imaginary indices of refraction for water (solid line) and ice (dotted line) over wavelengths ranging from 0.5 to 2.5 μm.

4. Radiative transfer model results for (a) the reflectance at 1.63 μm versus the reflectance at 0.65 μm for clouds composed of water droplets; (b) the reflectance at 2.15 μm versus the reflectance at 0.65 μm for clouds composed of water droplets; (c) the reflectance at 1.63 μm versus the reflectance at 0.65 μm for cirrus (ice) clouds; and (d) the reflectance at 2.15 μm versus the reflectance at 0.65 μm for cirrus (ice) clouds.

5. Radiative transfer model results for (a) the reflectance at 1.63 μm versus the brightness temperature at 11 μm for clouds composed of water droplets; (b) the reflectance at 2.15 μm versus the brightness temperature at 11 μm for clouds composed of water droplets; (c) the reflectance at 1.63 μm versus the brightness temperature at 11 μm for cirrus (ice) clouds; and (d) the reflectance at 2.15 μm versus the brightness temperature at 11 μm for cirrus (ice) clouds.

6. Radiative transfer model results for (a) the reflectance at 1.90 μm versus the brightness temperature at 11 μm for cold cirrus clouds as a function of optical thickness; and (b) the reflectance at 1.90 μm versus the brightness temperature at 11 μm for clouds composed of water droplets having r_{eff} = 4 μm as a function of optical thickness. VIS (0.65-μm) optical thicknesses range from 0 to 20 for the cirrus calculations and from 0 to 50 for the water cloud calculations.

7. Radiative transfer model results for cirrus [T = 234 K] overlying a water cloud [T = 284 K] having τ=5 and r_{eff} = 4 μm. (a) the reflectance at 1.63 μm versus the 11 μm brightness temperature; (b) the reflectance at 2.15 μm versus the 11 μm brightness temperature; (c) BTD[8.5-11 μm] versus the 11-μm brightness temperature; and (d) BTD[11-12 μm] versus the 11-μm brightness temperature.

8. MAS image recorded on April 21, 1996 over Oklahoma during ER-2 Flight Leg #11 at 2000 UTC. The data in the image represent an imager swath of 37.5 km in width by 50 km in length. Shown are (a) the scene at 0.65 μm; (b) the scene at 1.9 μm; and (c) the results of the MAS cloud clearing algorithm.

9. Discrimination of cloud thermodynamic phase from application of (a) the MODIS IR trispectral algorithm, (b) the MODIS IR trispectral method augmented by data from the 0.65, 1.63, and 1.90-μm channels.

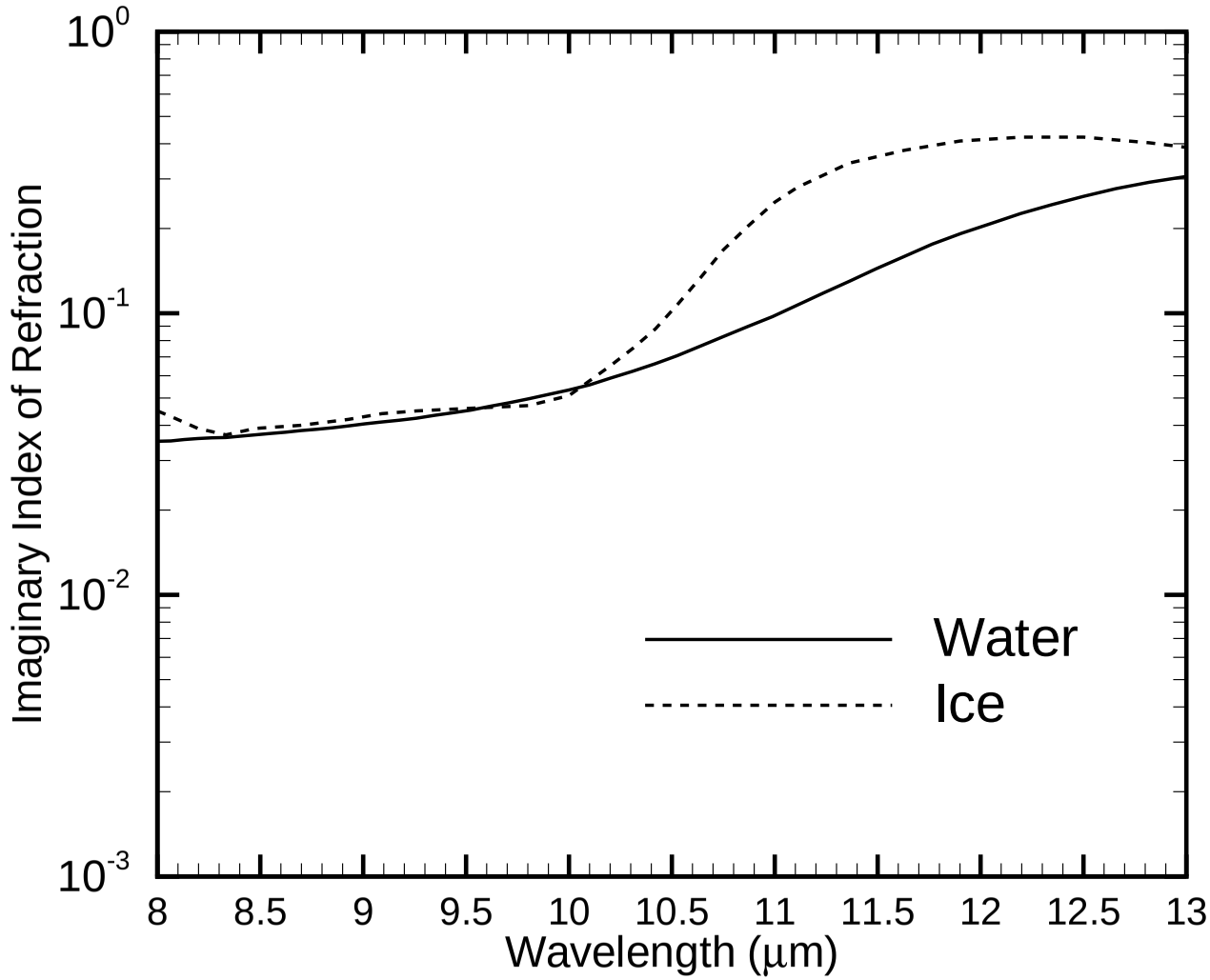
Imaginary Index of Refraction
10^0
10^{-1}
10^{-2}
10^{-3}
8
8.5
9
9.5
10
10.5
11
11.5
12
12.5
13
Wavelength (μm)
Water
Ice

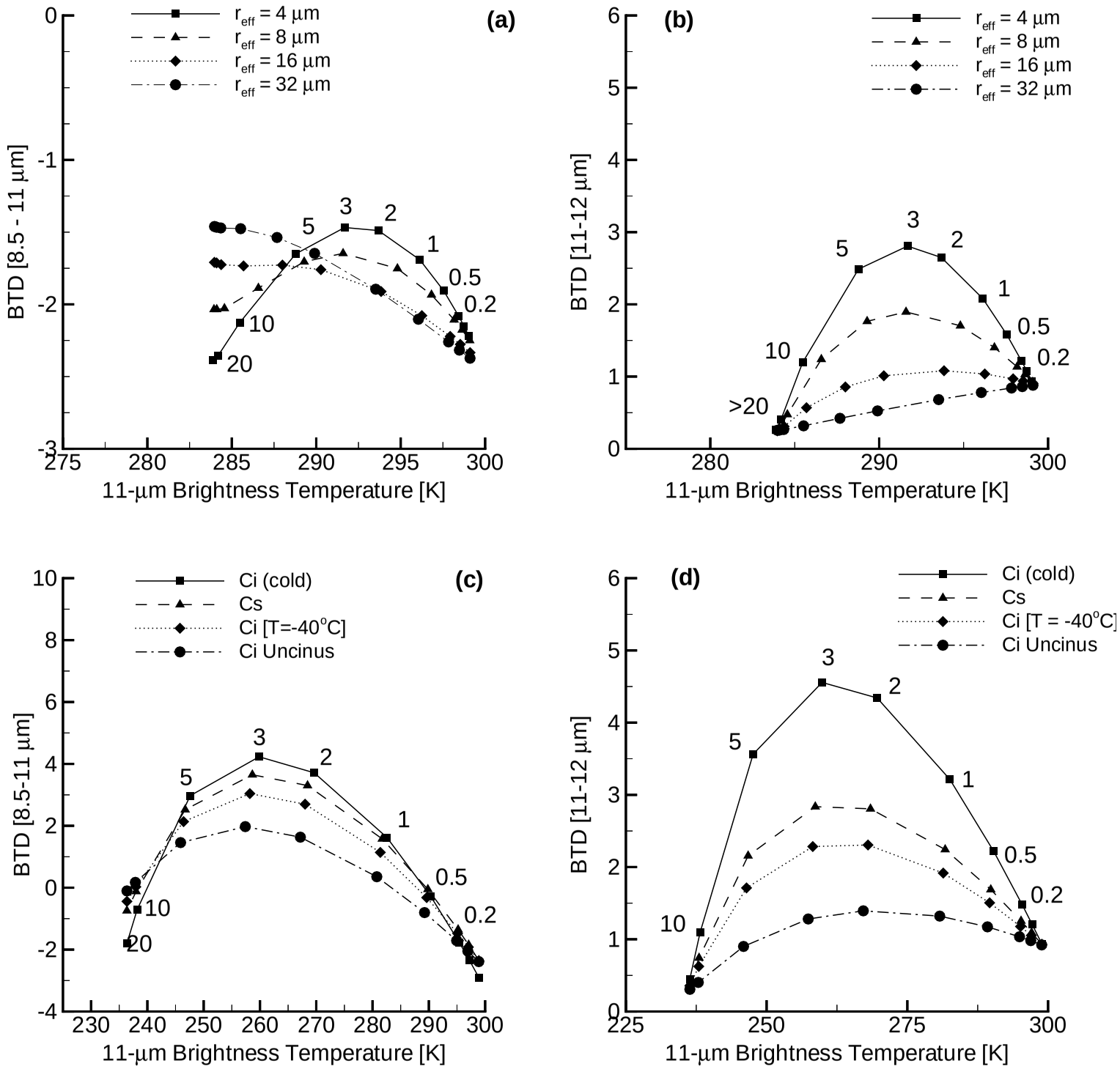
(a)
r_{eff} = 4 μm
r_{eff} = 8 μm
r_{eff} = 16 μm
r_{eff} = 32 μm
BTD [8.5 - 11 μm]
11-μm Brightness Temperature [K]
(b)
BTD [11-12 μm]
>20
(c)
Ci (cold)
Cs
Ci [T=-40°C]
Ci Uncinus
BTD [8.5-11 μm]
(d)
Ci [T = -40°C]

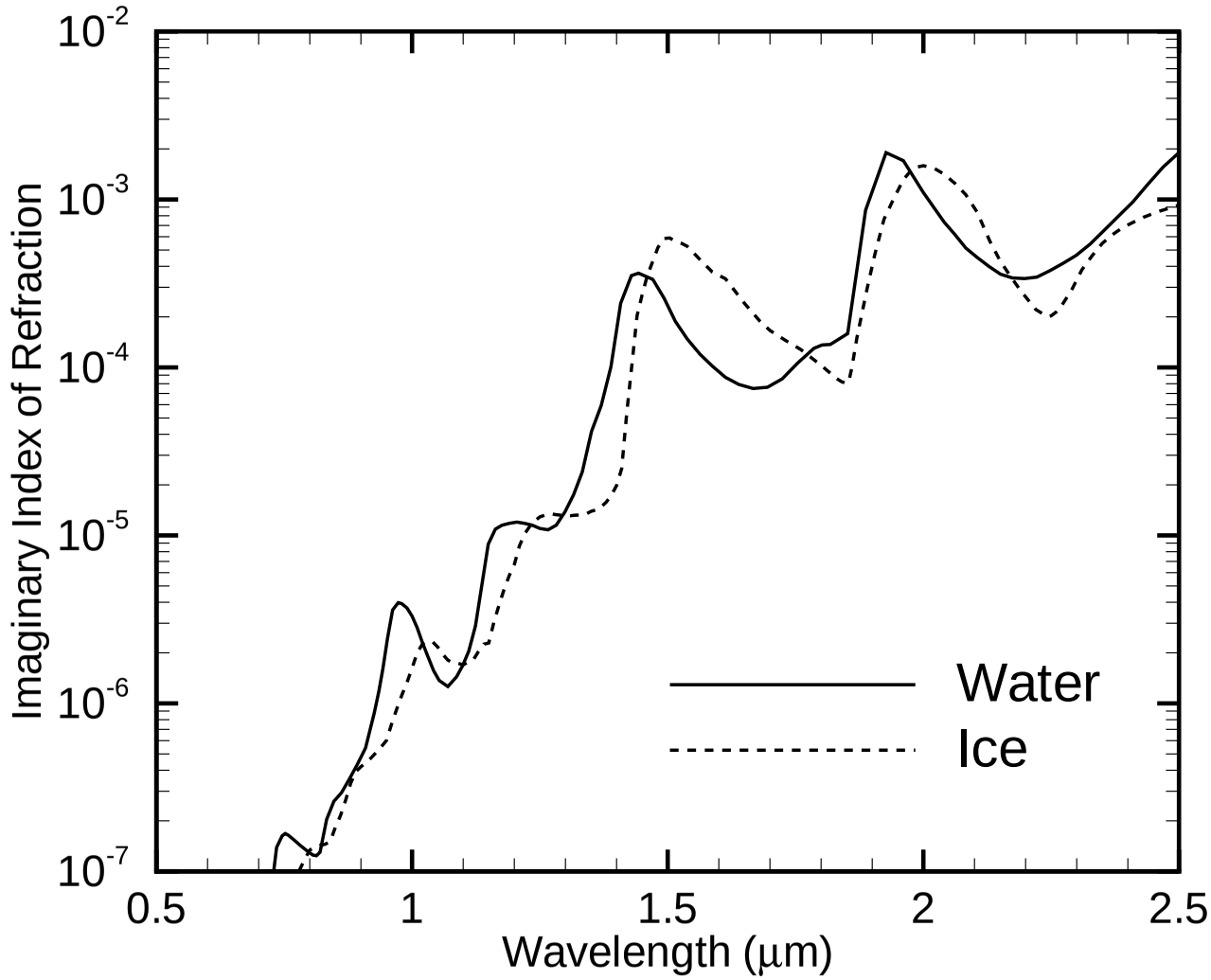
Imaginary Index of Refraction
10-2
10-3
10-4
10-5
10-6
10-7
0.5
1
1.5
2
2.5
Wavelength (μm)
Water
Ice

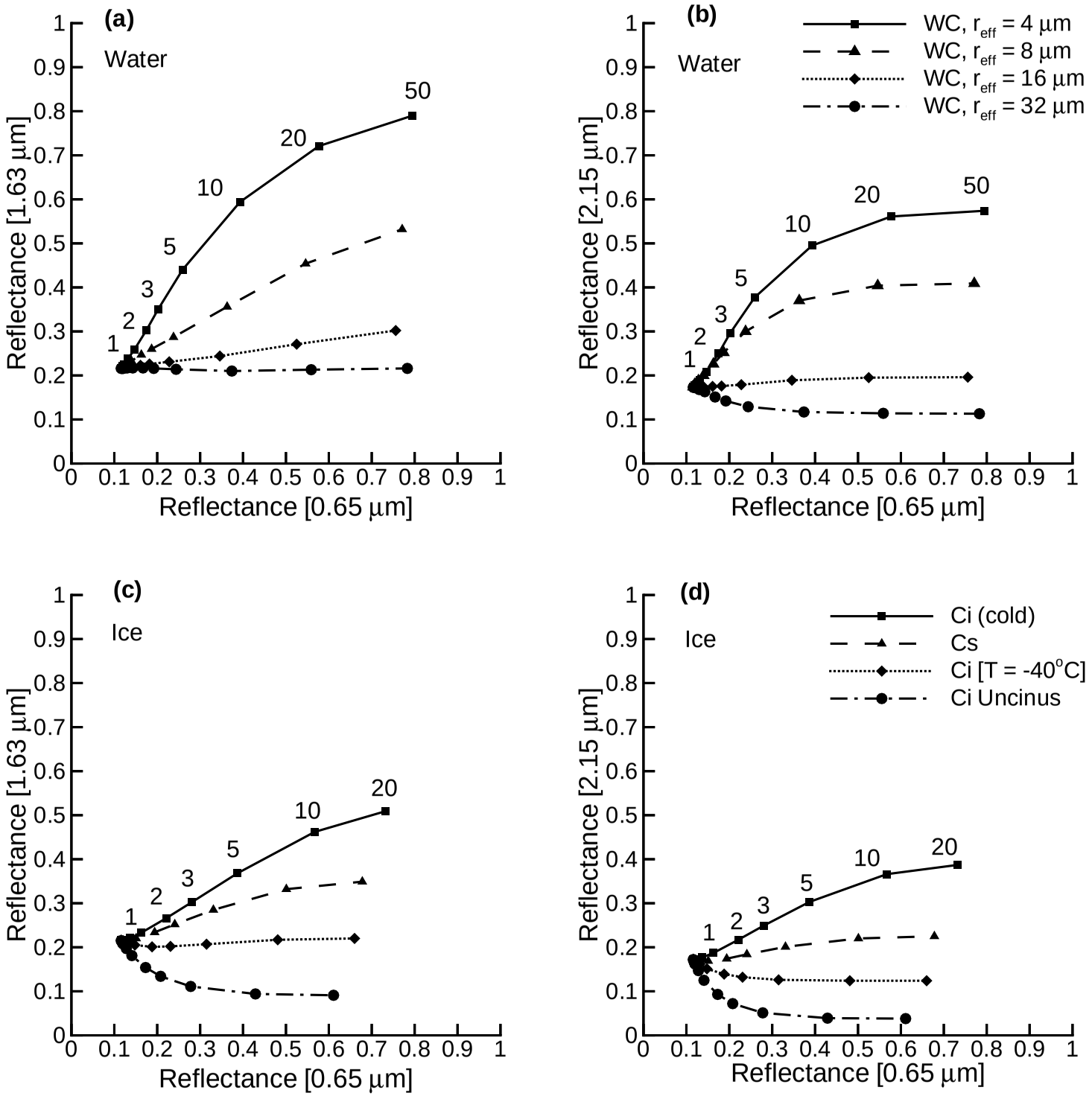
(a)
Water
(b)
Water
(c)
Ice
(d)
Ice
WC, r_{eff} = 4 μm
WC, r_{eff} = 8 μm
WC, r_{eff} = 16 μm
WC, r_{eff} = 32 μm
Ci (cold)
Cs
Ci [T = -40°C]
Ci Uncinus
Reflectance [1.63 μm]
Reflectance [2.15 μm]
Reflectance [0.65 μm]
1
2
3
5
10
20
50

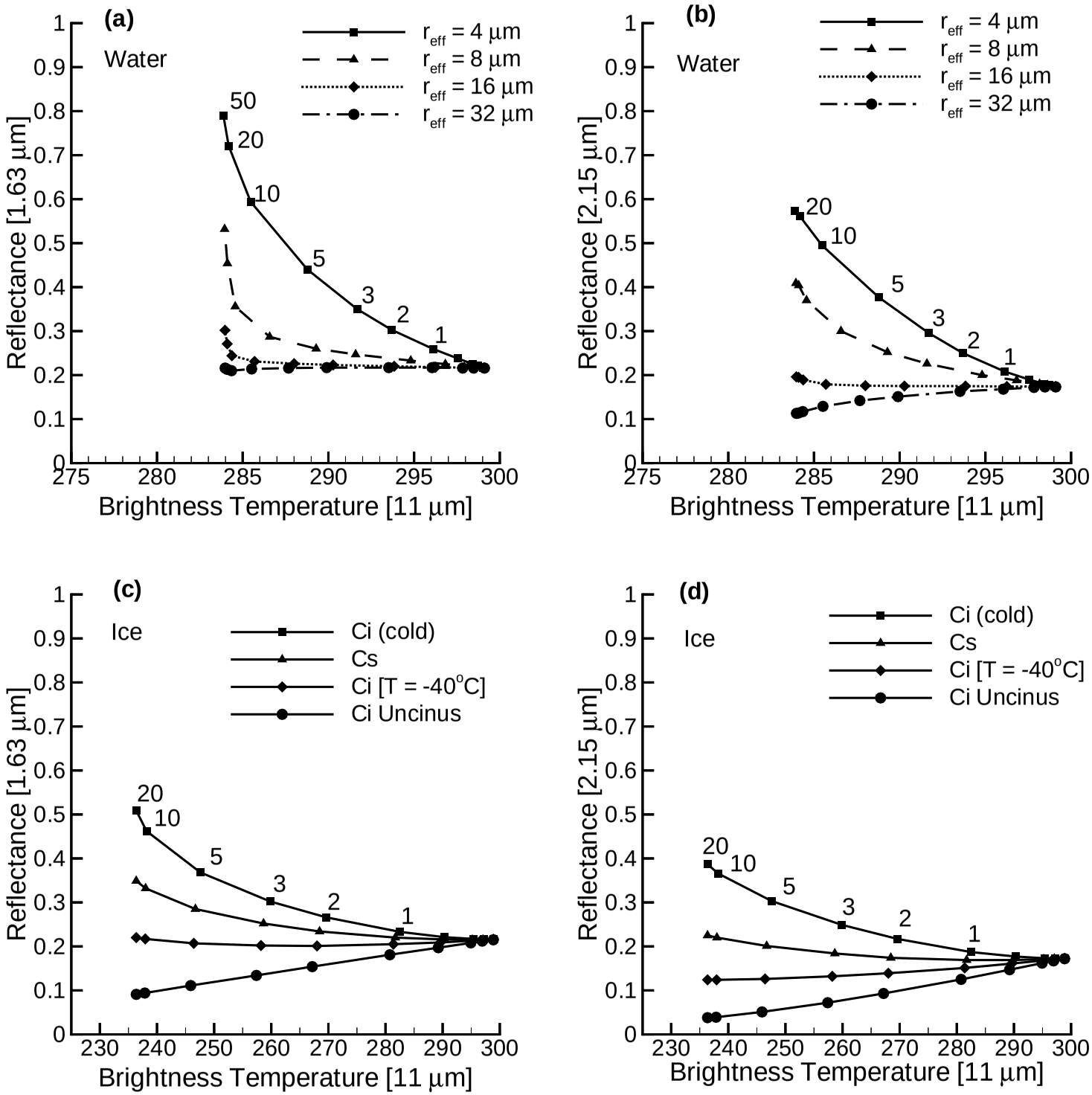
(a)
Water
r_{eff} = 4 μm
r_{eff} = 8 μm
r_{eff} = 16 μm
r_{eff} = 32 μm
50
20
10
5
3
2
1
Reflectance [1.63 μm]
Brightness Temperature [11 μm]
(b)
Water
r_{eff} = 4 μm
r_{eff} = 8 μm
r_{eff} = 16 μm
r_{eff} = 32 μm
20
10
5
3
2
1
Reflectance [2.15 μm]
Brightness Temperature [11 μm]
(c)
Ice
Ci (cold)
Cs
Ci [T = -40°C]
Ci Uncinus
20
10
5
3
2
1
Reflectance [1.63 μm]
Brightness Temperature [11 μm]
(d)
Ice
Ci (cold)
Cs
Ci [T = -40°C]
Ci Uncinus
20
10
5
3
2
1
Reflectance [2.15 μm]
Brightness Temperature [11 μm]

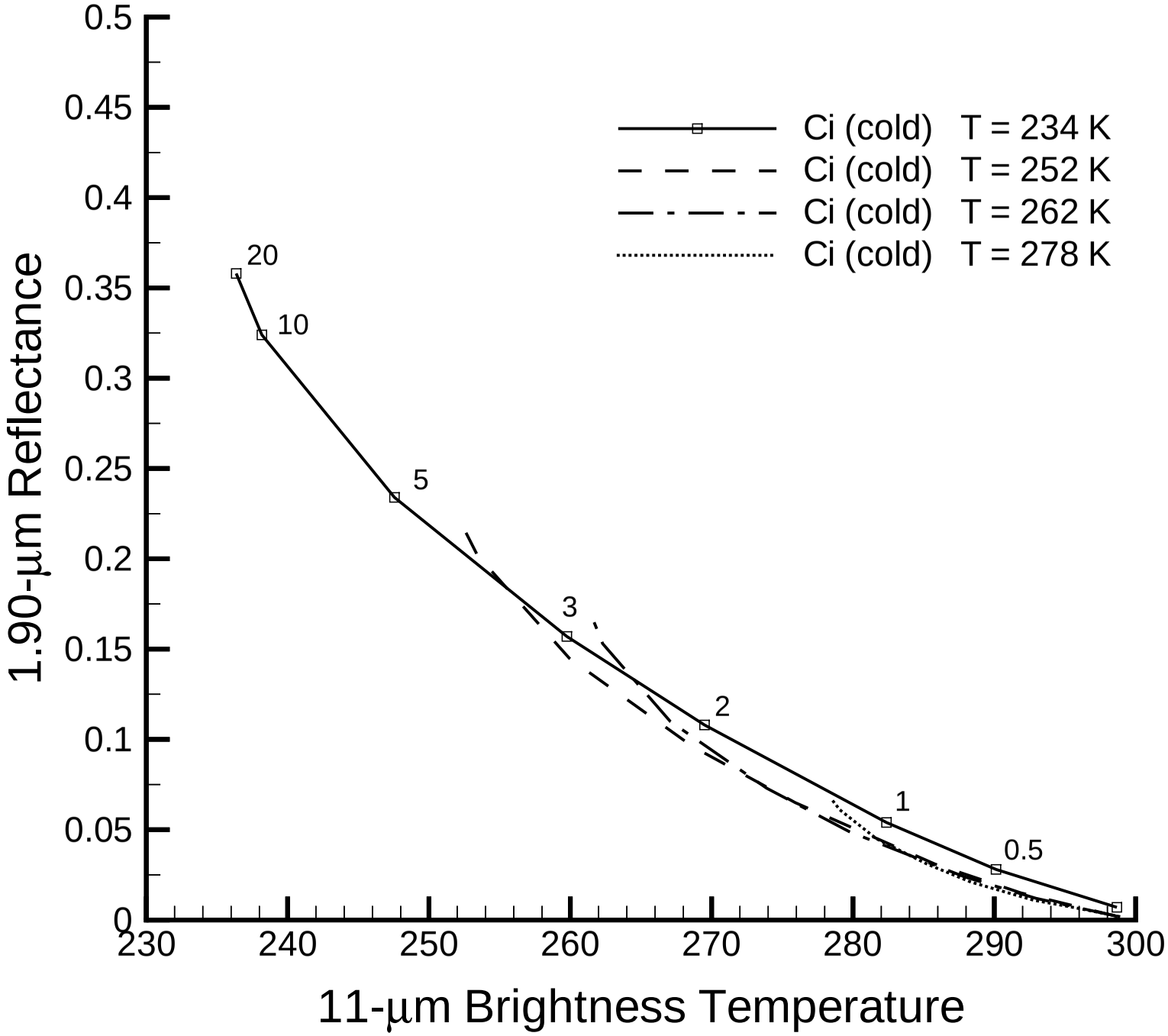
Ci (cold) T = 234 K
Ci (cold) T = 252 K
Ci (cold) T = 262 K
Ci (cold) T = 278 K
20
10
5
3
2
1
0.5
0.5
0.45
0.4
0.35
0.3
0.25
0.2
0.15
0.1
0.05
0
230
240
250
260
270
280
290
300
1.90-µm Reflectance
11-µm Brightness Temperature

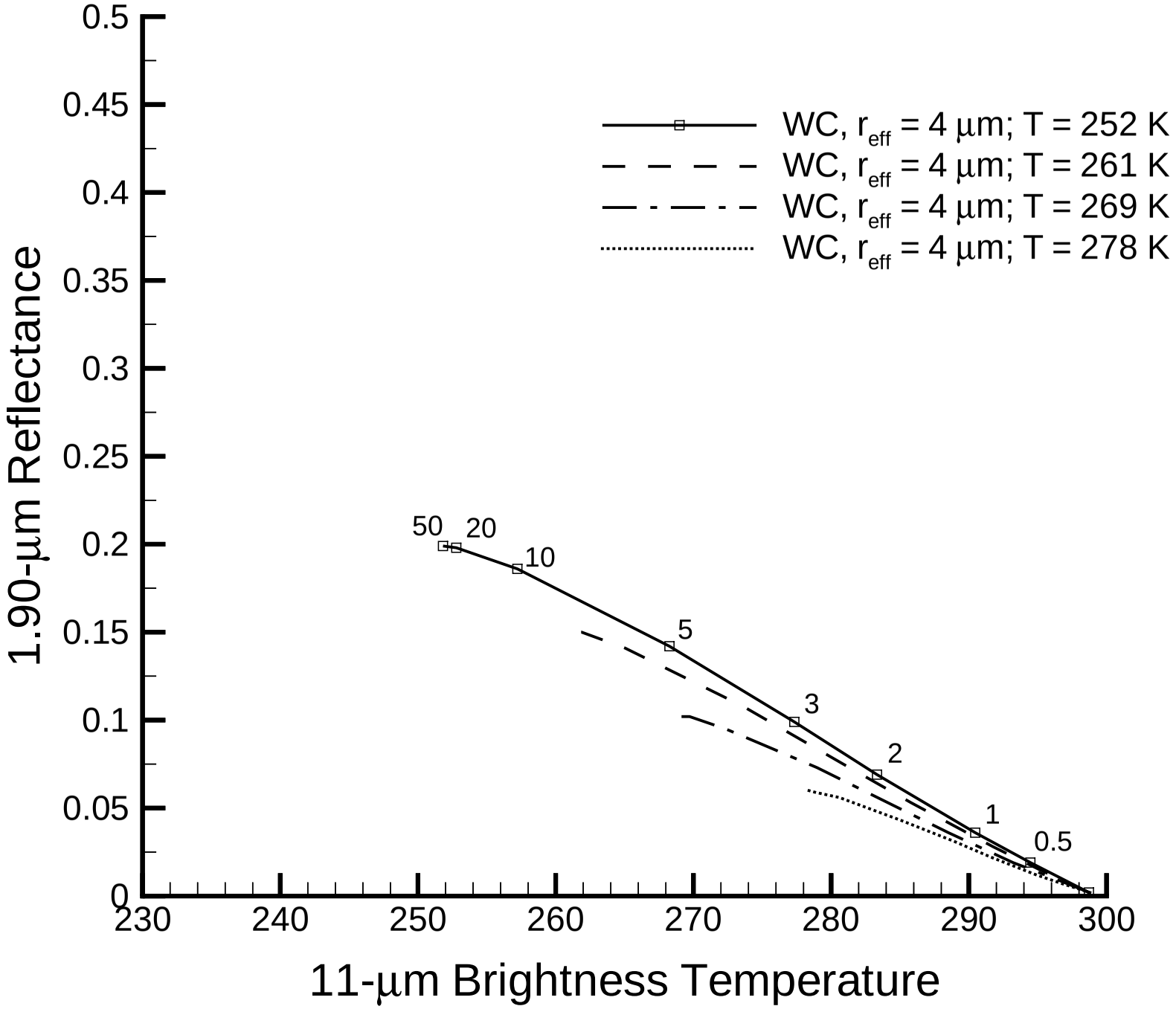
WC, r_{eff} = 4 μm; T = 252 K
WC, r_{eff} = 4 μm; T = 261 K
WC, r_{eff} = 4 μm; T = 269 K
WC, r_{eff} = 4 μm; T = 278 K
1.90-μm Reflectance
11-μm Brightness Temperature
0
0.05
0.1
0.15
0.2
0.25
0.3
0.35
0.4
0.45
0.5
230
240
250
260
270
280
290
300
50
20
10
5
3
2
1
0.5

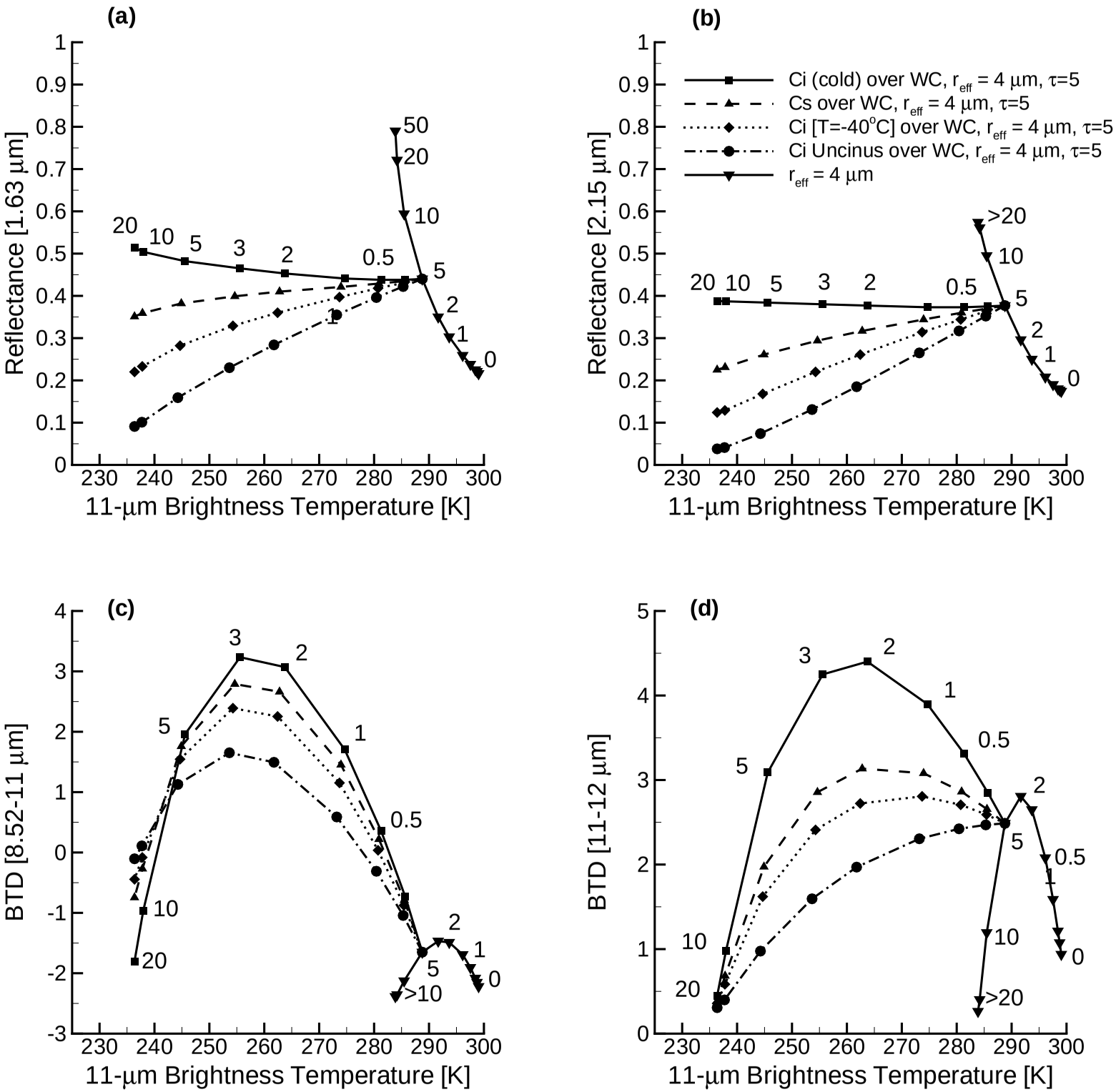
(a)
Reflectance [1.63 µm]
11-µm Brightness Temperature [K]
(b)
Reflectance [2.15 µm]
11-µm Brightness Temperature [K]
Ci (cold) over WC, r_{eff} = 4 µm, τ=5
Cs over WC, r_{eff} = 4 µm, τ=5
Ci [T=-40°C] over WC, r_{eff} = 4 µm, τ=5
Ci Uncinus over WC, r_{eff} = 4 µm, τ=5
r_{eff} = 4 µm
(c)
BTD [8.52-11 µm]
11-µm Brightness Temperature [K]
(d)
BTD [11-12 µm]
11-µm Brightness Temperature [K]

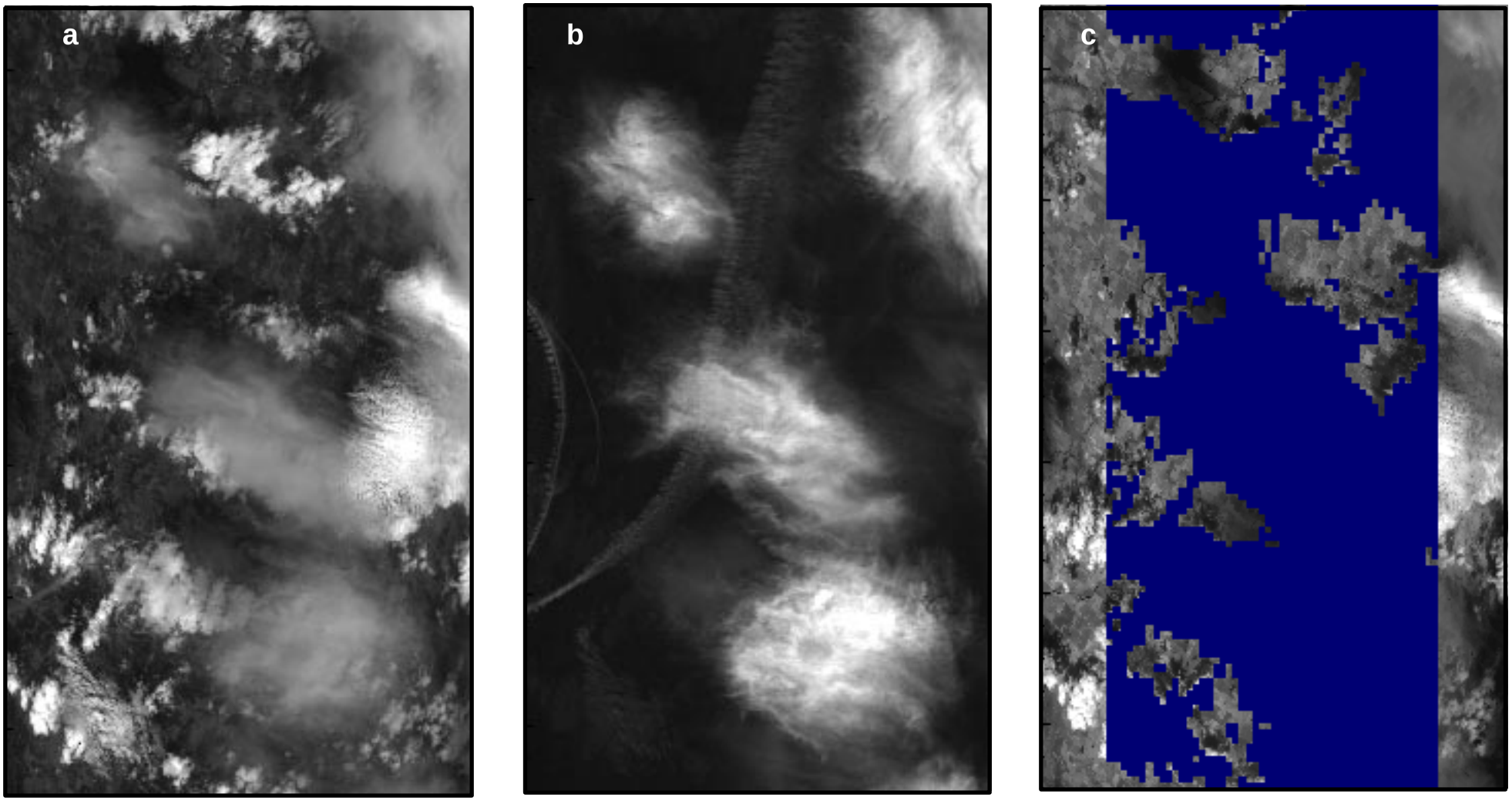

0.65 μm **1.90 μm** **MAS Cloud Mask Result**

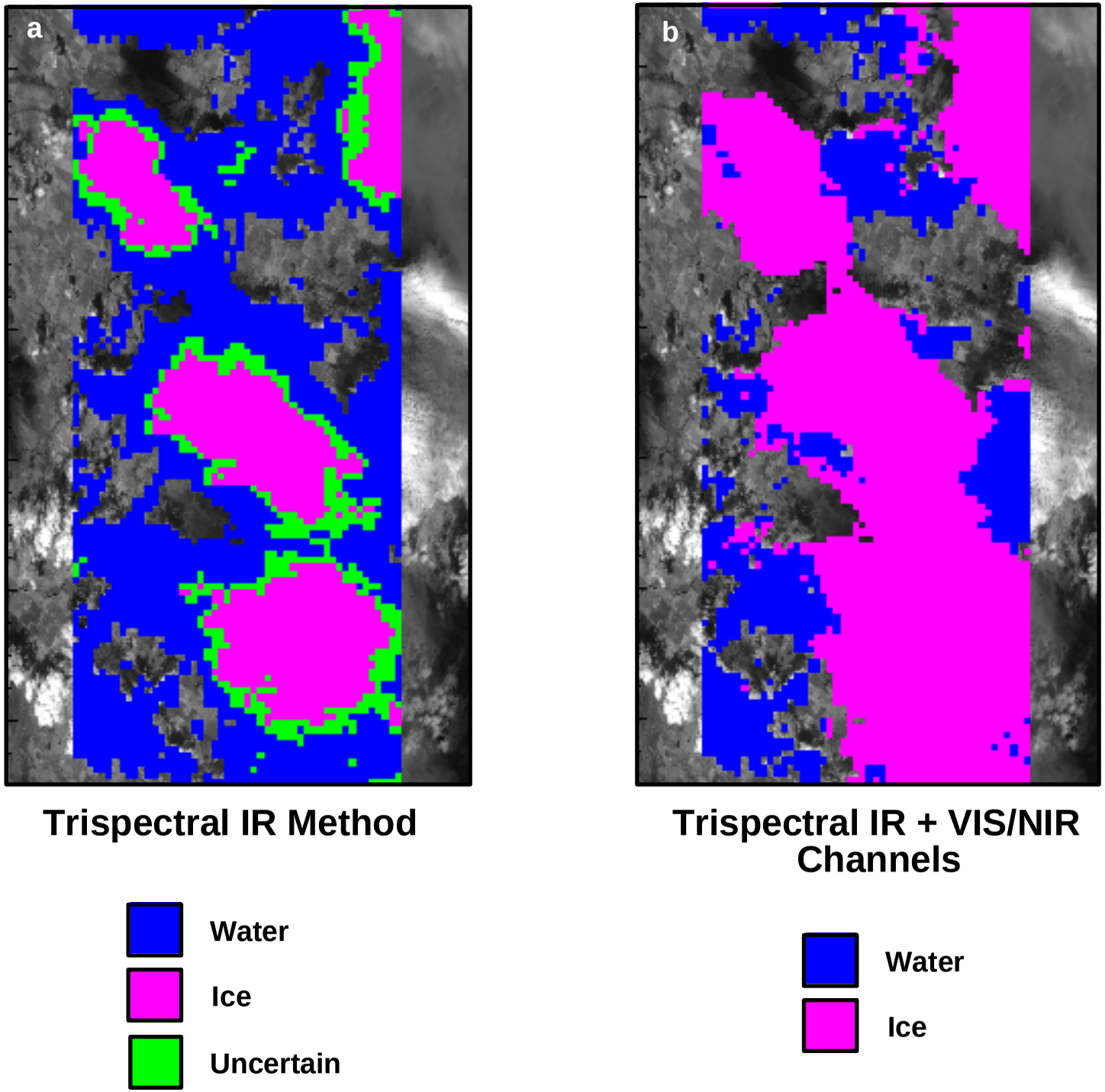
a
b
Trispectral IR Method
Trispectral IR + VIS/NIR Channels
Water
Ice
Uncertain
Water
Ice